RSC Medicinal Chemistry

RESEARCH ARTICLE

Cite this: RSC Med. Chem., 2025, 16, 6081

Design and synthesis of enantiopure NHC–silver(I) and NHC–gold(I) complexes with anticancer, anti-inflammatory and antioxidant properties

Domenico Iacopetta, [a] Assunta D'Amato, *[b] Jessica Ceramella,[a] Annaluisa Mariconda, [c] Camillo Rosano,*[d] Maria Marra,[a] Alessia Catalano,[e] Pasquale Longo†[b] and Maria Stefania Sinicropi†[a]

Received 24th July 2025,
Accepted 23rd September 2025

DOI: 10.1039/d5md00651a

rsc.li/medchem

So far, several interesting reports dealing with *N*-heterocyclic carbene (NHC) complexes bearing silver and gold have been published, highlighting their versatility in several research fields and their various applications as well. However, most of the reported NHC complexes have been synthetically obtained and studied as racemates, whereas less is still known about the properties of enantiopure complexes. Aiming at contributing to fill this gap, herein a new series of enantiopure NHC complexes of silver(I) and gold(I) bearing an imidazole derivative, opportunely substituted, with one or two asymmetric carbons has been synthesized. These complexes have been characterized by ^{1}H and ^{13}C NMR, mass spectrometry, and elemental analysis and studied for their anticancer, anti-inflammatory and antioxidant properties. The most active complex was also further investigated for its ability in modulating two main enzymes involved in cancer and inflammatory diseases, *viz.* human topoisomerase I (hTopoI) and murine inducible nitric oxide synthase (iNOS). The outcomes highlight the role of the configuration and substituents in the regulation of the above-mentioned targets, strengthening the need to widen the studies on enantiopure NHC complexes, which may represent useful compounds to be further developed for the obtaining of tailored therapeutic regimens.

Introduction

Chirality plays a main role in drug affinity and interactions toward a given biological target, so that one enantiomer may become clinically more effective, possessing a safer and more selective profile compared to its racemate.[1] Consequently, chiral drugs became a challenging issue in the design, synthesis and development of new drugs to be employed for treating different diseases. It is clear that the use of enantiopure drugs offers some advantages over the administration of racemic mixtures.[2]

N-heterocyclic carbene (NHC) ligands and their metal complexes have gained the attention of many researchers because of their chemical and biological properties. In this scenario, several efforts have been made for the development of chiral NHC–metal complexes, which found several applications not only in asymmetric synthesis/catalysis but also in medicinal chemistry.[3,4] Over time, several interesting results were disclosed in this area of research, and NHC–metal complexes have become powerful candidates for the treatment of various diseases.[5–7] Different biological targets regulated by NHC–metal complexes were also investigated, corroborating their versatility and effectiveness as, for instance, thioredoxin reductase (TrxR), human topoisomerases, cyclooxygenases and so on.[8,9] In the last decade, we focused our research activity on the design of gold and silver complexes stabilized by NHC ligands, in order to study the ability of these compounds in numerous catalytic and medicinal chemistry applications. To achieve these results, we developed tunable synthetic routes to obtain functionalized N-heterocyclic ligands containing methyl and alcohol side arms, starting from various imidazole derivatives with hydrogen, chloride, phenyl, xanthine, or a condensed benzene ring on the backbone. The substituents on the backbone of the imidazole ring strongly influence the σ-donation of the carbene to the

[a] *Department of Pharmacy, Health and Nutritional Sciences, University of Calabria, Via Pietro Bucci, 87036 Arcavacata di Rende, Italy*
[b] *Department of Chemistry and Biology "A. Zambelli", University of Salerno, Via Giovanni Paolo II 132, 84084 Fisciano, Italy. E-mail: asdamato@unisa.it*
[c] *Department of Basic and Applied Sciences (DISBA), University of Basilicata, Via Dell'Ateneo Lucano 10, 85100, Potenza, Italy*
[d] *Proteomics and Mass Spectrometry Unit, IRCCS Ospedale Policlinico San Martino, Largo Rosanna Benzi, 10, 16132 Genova, Italy. E-mail: camillo.rosano@hsanmartino.it*
[e] *Department of Pharmacy-Drug Sciences, University of Bari "Aldo Moro", Via Orabona, 4, 70126 Bari, Italy*
† Co-senior authors.

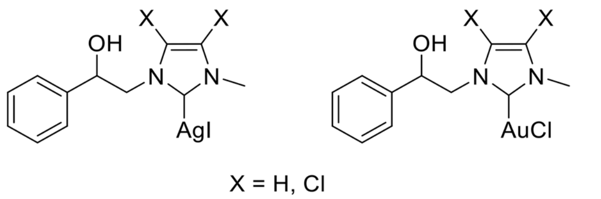

Fig. 1 NHC–Ag(I) and NHC–Au(I) complexes previously reported.

metal and, therefore, the stability of the resulting complex, as well as its lipophilicity.

The synthesized complexes have a substituent on one of the nitrogen atoms of the NHC ligand that possesses a stereogenic center (Fig. 1), but the used reagents produced a racemic mixture; thus, they were tested as racemates.[10–12]

However, since single enantiomers can exhibit significant different pharmacodynamic, pharmacokinetic, and toxicological properties, the resolution of racemic mixtures or enantiospecific synthesis are particularly important in developing new, more effective, and safer drugs.

Recently, we separately synthesized the *R*- and *S*-enantiomers of the silver and gold NHC complexes shown in Fig. 1 and studied their biological activity. In particular, we evaluated their anticancer, antibacterial, and anti-inflammatory properties. The obtained results, *in silico* and *in vitro*, showed that one of the two enantiomers was more active and selective.[4]

The previously obtained results have strengthened the idea that enantiopure NHC complexes based on gold and silver can be extremely useful for the development of increasingly effective multitarget drugs. Thus, in the present work, we synthesized and characterized by ^{1}H and ^{13}C NMR, mass spectrometry, and elemental analysis new enantiopure NHC complexes of silver and gold having an imidazole derivative containing substituents with an asymmetric carbon, namely the 2-phenylethyl group (see Scheme 1). The new series of enantiopure NHC–Ag(I) and NHC–Au(I) complexes were studied for their anticancer, anti-inflammatory and antioxidant properties. Particularly, the obtained outcomes highlighted that the gold-based complexes possessed a better anticancer activity than the silver-based ones and that it depends on the configuration and the nature of the NHC substituents. A similar trend was found for the anti-inflammatory and antioxidant properties. Additionally, two important targets, namely the human topoisomerase I and the inducible nitric oxide synthase (iNOS), implicated in the onset of cancer and inflammatory diseases, were found to be regulated by the most active member of this new series of enantiopure complexes. The obtained data revealed interesting differences related to the complexes' configuration and to the different substituents of the carbenic core, with the latter responsible for their different lipophilicity. These studies provide new insights into the importance of the design and synthesis of suitably substituted enantiopure molecules, and their relationships with biological effects which can lay the groundwork for further development in clinical applications.

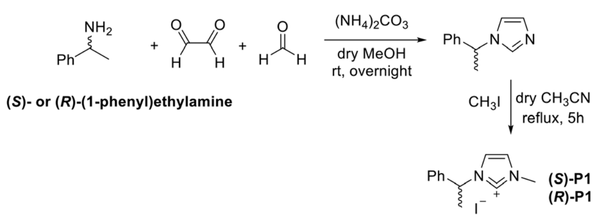

Scheme 1 Synthesis of enantiopure proligands (*S*)-P1/(*R*)-P1.

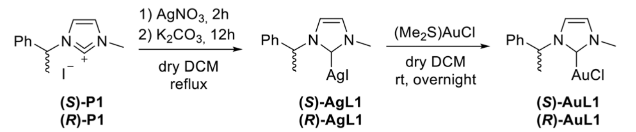

Scheme 2 Synthesis of enantiopure silver complexes (*S*)-AgL1/(*R*)-AgL1 and enantiopure gold complexes (*S*)-AuL1/(*R*)-AuL1.

Results and discussion

Chemistry

Similarly to the best performing typical *N*-heterocyclic carbene (NHC) ligand previously reported by us,[10,13] we designed ligands **(*S*)-P1**/**(*R*)-P1**, bearing one methyl substituent on the N^3 imidazole atom, and one enantiopure 2-phenylethyl moiety on the N^1 atom. The synthesis was accomplished in an efficient one-pot procedure by reacting glyoxal with (*S*)- or (*R*)-2-phenylethylamine and achieving ring closure in the presence of *p*-formaldehyde (Scheme 1).[14] Subsequent methylation with iodomethane under our optimized reaction conditions[10] led to proligands **(*S*)-P1**/**(*R*)-P1**.

N-heterocyclic carbene was achieved in an alkaline environment due to K_2CO_3, and metalation was performed in the presence of silver nitrate as the metal source to obtain complexes **(*S*)-AgL1**/**(*R*)-AgL1**, which were lastly subjected to transmetalation with $(Me_2S)AuCl$ to gain Au(I) analogous **(*S*)-AuL1**/**(*R*)-AuL1** (Scheme 2).[13]

Then, we decided to investigate the influence of an increase in lipophilicity and, at the same time, the presence of a double stereogenic center on the NHC ligand, by switching from the methyl substituent on the N_3 atom with an additional 2-phenylethyl unit. Proligands **(*S*)-P2**/**(*R*)-P2** were synthesized according to literature procedures,[15] by a convenient one-pot reaction, similarly to chiral mono-substituted imidazolium salts **(*S*)-P2**/**(*R*)-P2**, obviously employing two equivalents of the desired chiral amine, glyoxal and *p*-formaldehyde (Scheme 3).

This time, the silver complexes were obtained by a reaction with silver oxide in an anhydrous environment.[15] The analogous gold complexes were attained through transmetalation with $(Me_2S)AuCl$ (Scheme 4).

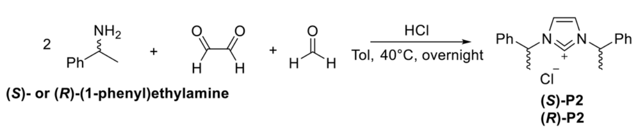

Scheme 3 Synthesis of enantiopure proligands (*S*)-P2/(*R*)-P2.

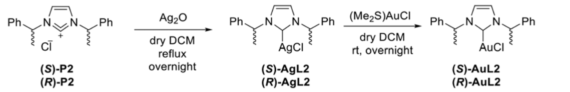

Scheme 4 Synthesis of enantiopure silver complexes (*S*)-AgL2/(*R*)-AgL2 and enantiopure gold complexes (*S*)-AuL2/(*R*)-AuL2.

Table 1 Specific rotation ($[\alpha]^{D}_{25}$) of complexes (*S*)-ML1-2/(*R*)-ML1-2

Compound	$[\alpha]^{D}_{25}$ (C = 0.5, $CHCl_3$)
(*S*)-AgL1	+98.6
(*R*)-AgL1	−101.3
(*S*)-AuL1	+109.5
(*R*)-AuL1	−108.3
(*S*)-AgL2	+88.6
(*R*)-AgL2	−87.2
(*S*)-AuL2	+123.7
(*R*)-AuL2	−121.2

All the novel-synthesized molecules were thoroughly characterized *via* NMR spectroscopy and mass spectrometry. Moreover, polarimetric analysis confirmed the opposite configuration at the superimposed stereogenic centers (Table 1).

Anticancer activity

The anticancer activity of the new series of enantiopure NHC complexes, bearing one or two chiral centers (**L1** and **L2** series, respectively), was determined adopting two breast cancer cell lines, which are the triple negative MDA-MB-231 and the ER-α positive MCF-7 cells, using the MTT assay. As a normal counterpart, the human mammary epithelial MCF-10A cells were also assayed, in order to determine the selectivity. Table 2 shows the calculated IC_{50} values and the relative selectivity index for each molecule.

At first sight, it is clearly evident that the most active enantiopure complexes were found to be those bearing gold as the metal, with respect to the silver ones. However, the configuration seems to strictly influence the activity and, mainly, the selectivity. Indeed, the most active candidate, in both the cell models adopted, was **(*S*)-AuL1**, with IC_{50} values of 0.5 ± 0.1 and 1.7 ± 0.1 μM for MDA-MB-231 and MCF-7 cells, respectively. This complex was also found high selective toward both the breast cancer cell lines, with respect to the normal counterpart, as shown in Table 2. However, a net drop in both anticancer activity and selectivity was observed for its enantiomer, **(*R*)-AuL1**. This is not surprising, since it is generally known that one enantiomer can be bioactive and the opposite inactive, less active or also responsible for unwanted effects.[16] In the present case, this is a further validation of the importance to design and obtain enantiopure metal complexes for selective and safer drug development. Next, the corresponding silver bearing enantiopure complexes, **(*S*)-** and **(*R*)-AgL1**, were found to possess a lesser activity than the above-mentioned gold complexes, mostly against the MDA-MB-231 cells, where **(*S*)-AgL1** was totally inactive and **(*R*)-AgL1** exhibited an IC_{50} value of 20.6 ± 1.4 μM. A higher, but inverted, activity was found in MCF-7 cells, whereas a similar ability in impairing the MCF-10A cell viability was recorded (Table 2). Finally, both the pro-ligands, **(*S*)-** and **(*R*)-P1**, were tested and the obtained results clearly confirm that the configuration of the pro-ligands, and consequently of the relative complexes, is definitely determinant for the activity and selectivity, since **(*R*)-P1** was found more cytotoxic toward all the adopted cell lines, opposite to **(*S*)-P1**. The **L2** series structurally differentiate for the presence of two chiral carbons on the NHC ligand and for the substituent at the N in position 3, which increased the lipophilicity. These molecules produced different results, and indeed both the enantiopure pro-ligands **(*S*)-** and **(*R*)-P2** affected the MCF-10A cell viability in a similar way and were already more cytotoxic than **(*S*)-** and **(*R*)-P1** (Table 2). The above-mentioned pro-ligands influence, consequently, the behavior of the corresponding silver and gold complexes, as the selectivity lowered, overall, with respect to the **L1** series, with the exception of **(*S*)-AgL2** in MCF-7 cells and **(*R*)-AuL2** in both cell lines. As the reference drug in these experiments, cisplatin was included. However, it is less effective and selective compared to the identified leads (Table 2). Summing up, the obtained outcomes suggest that the metal, the

Table 2 IC_{50} values of metal complexes and pro-ligands, expressed as μM. The means ± standard deviations are shown

IC_{50} (μM)				SI	
	MDA-MB-231	MCF-7	MCF-10A	MDA-MB-231	MCF-7
(*S*)-P1	86.95 ± 7.6	>100	>100	>1.2	>1
(*R*)-P1	71.0 ± 6.8	34.0 ± 2.4	40.3 ± 3.6	0.6	1.2
(*S*)-AgL1	>100	7.5 ± 0.8	77.1 ± 6.8	>0.8	10.3
(*R*)-AgL1	20.6 ± 1.4	11.2 ± 0.6	72.8 ± 5.8	3.5	6.1
(*S*)-AuL1	0.5 ± 0.1	1.7 ± 0.1	11.5 ± 0.5	21.2	6.5
(*R*)-AuL1	5.8 ± 0.5	6.8 ± 0.4	2.1 ± 0.1	0.4	0.3
(*S*)-P2	10.8 ± 1.1	16.3 ± 1.3	28.8 ± 1.9	2.7	1.8
(*R*)-P2	>100	58.0 ± 4.3	28.2 ± 1.9	0.3	0.5
(*S*)-AgL2	14.3 ± 1.2	4.2 ± 0.3	24.0 ± 1.1	1.7	5.8
(*R*)-AgL2	17.6 ± 1.7	9.7 ± 0.8	24.8 ± 1.7	1.4	2.6
(*S*)-AuL2	2.3 ± 0.1	1.8 ± 0.1	5.3 ± 0.2	2.3	2.8
(*R*)-AuL2	6.9 ± 0.3	7.0 ± 0.6	7.1 ± 0.5	1.0	1.0
Cisplatin	29.5 ± 0.9	37.3 ± 1.2	79.4 ± 1.6.	2.7	2.1

complexes' configuration, the presence of one or two chiral centers and the varied lipophilicity strongly influence the activity and selectivity of the enantiopure complexes, in the adopted cellular models.

Human topoisomerase I assay

It is known that NHC–metal complexes possess many pharmaceutical activities, exerted through the modulation of numerous biological pathways and key-point targets.[17] However, the biological properties of enantiopure NHC–gold and NHC–silver complexes are quite an unexplored field, and especially the investigation of the possible interactions with biological targets involved in sundry diseases is a very interesting and growing scientific field. Considering the viability assay outcomes, we focused our attention on both the enantiomers (***S***)- and (***R***)-**AuL1**, aiming at further investigating the anticancer properties. With this purpose, both the enantiopure complexes were tested for their ability to modulate the hTopoI, an enzyme that our research group has studied for a long time and that was the target of different metal complexes, acting as inhibitors.[18] Most importantly, these experiments were performed not only for investigating this cellular target that can be tuned by (***S***)- and (***R***)-**AuL1**, but also for studying the behavior of the enantiomers toward this enzyme, in order to establish a model to be used for obtaining new and selective anticancer drugs. Therefore, for determining the capability of (***S***)- and (***R***)-**AuL1** to block the relaxation of supercoiled DNA activity of hTopoI, an *in vitro* assay was employed, exposing the enzyme to increasing concentrations of both the enantiopure complexes. The achieved outcomes, shown in Fig. 2, revealed that the enantiomers inhibited the hTopoI depending on the adopted concentration, suggesting a different affinity for the enzyme.

Indeed, (***R***)-**AuL1** had a better inhibitory activity than (***S***)-**AuL1**, considering that it was able to totally block the relaxation of the supercoil DNA substrate (pHOT1) already at the concentration of 0.01 μM (lane 6), as the evidenced by the net band of uncut DNA in the lowest area of the gel, and partially at 0.001 μM (lane 4). The inhibitory activity was, obviously, preserved at higher concentrations (0.1 and 1 μM, lanes 8 and 10 respectively). In contrast, (***S***)-**AuL1** totally inhibited the enzyme only at the higher concentration (1 μM, lane 9), and partially and dose-dependently at the lower concentrations (0.01 and 0.1 μM, lanes 5 and 7, respectively), whereas no inhibition was observed at the lowest concentration (0.001 μM, lane 3). Indeed, in the latter case, the DNA was cut by the enzyme producing a pattern similar to that of the control reaction (lane 2), in which the fully active enzyme was exposed only to the vehicle (DMSO). Lane 1 shows the uncut supercoiled DNA plasmid, used as the negative control. It should be highlighted that (***S***)-**AuL1** was found the most active and selective toward the breast cancer cells in the viability assay, in contrast to (***R***)-**AuL1**, even though the latter was found to inhibit the hTopoI activity at a concentration 100 times lower than that of (***S***)-**AuL1**. However, this behavior could explain the difference in selectivity amongst the two enantiomers, because a higher affinity toward hTopoI could also impair the basal activity of the enzyme, which is not overexpressed in normal breast cells used as a control in previous assays, or may also have some off-target cytotoxicity.[19] Besides, the hTopoI is just one of the diverse targets that can be modulated by these complexes, and thus it is very likely that (***S***)-**AuL1** can impact other targets involved in cancer cell pathways and the synergistic effects can be responsible for the found activity and selectivity. Indeed, as demonstrated in the next experiments, (***S***)-**AuL1** has been found to also regulate the iNOS, in which abnormal activity has been strictly related to cancer onset and progression, affecting tumor heterogenicity, evolution and resistance to clinical treatment.[20] Finally, other mechanisms, for instance membrane cell permeation and/or efflux pumps (*e.g.* PgP or other multidrug resistance (MDR) proteins)[21] amongst all, may account for the diverse activity and selectivity exerted by the two complexes in the adopted cancer cell models.

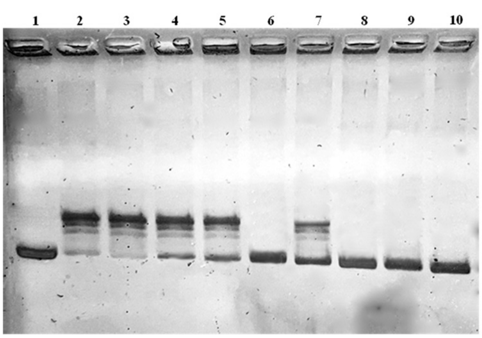

Fig. 2 hTopoI assay. Supercoiled DNA was incubated without or with the hTopoI in the absence or presence of the enantiopure gold complexes, at different concentrations. Lane 1: plasmid pHOT1; lane 2: control reaction (vehicle, DMSO); lanes 3, 5, 7 and 9: (***S***)-**AuL1** at 0.001, 0.01, 0.1 and 1 μM, respectively; lanes 4, 6, 8 and 10: (***R***)-**AuL1** at 0.001, 0.01, 0.1 and 1 μM, respectively.

Nuclear DNA damage

In our experience, the impact on MDA-MB-231 breast cancer cell viability and the proved inhibition of hTopoI exerted by the lead enantiopure complex (***S***)-**AuL1** could lead to the genomic DNA damage that, in turn, push cancer cells to die by the apoptotic mechanism. Indeed, a number of literature data inherent to racemic NHC–metal complexes, to which we contributed over the years, reported that the blockade of topoisomerases and nuclear DNA damage are strictly connected.[22,23] Thus, aiming at investigating whether (***S***)-**AuL1** could damage the nuclear DNA and induce cancer cell death by apoptosis, a TUNEL assay was performed on MDA-MB-231 cells. Briefly, cells were treated with (***S***)-**AuL1**, at a concentration equal to 1 μM, or DMSO (vehicle), for 24 h, then subjected to the TUNEL assay, as detailed in the

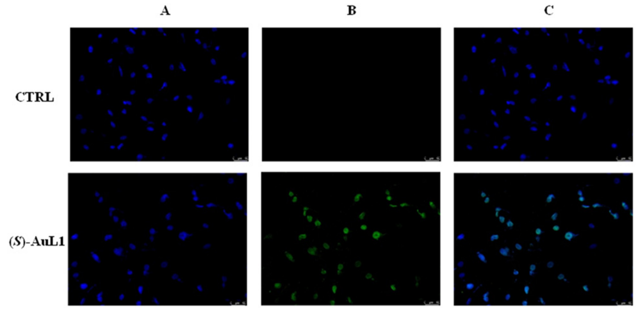

Fig. 3 MDA-MB-231 cells were subjected to TUNEL assay after treatment with 1 μM of **(*S*)-AuL1**, or DMSO (CTRL), for 24 h. Cells were observed and images were acquired at 20× magnification, using an inverted fluorescence microscope. The green fluorescence, visible only under **(*S*)-AuL1** treatment, highlights nuclear DNA damage. Panels A: DAPI (CTRL and **(*S*)-AuL1**) excitation/emission wavelength 350 nm/460 nm. Panels B: CF™488A (CTRL and **(*S*)-AuL1**) excitation/emission wavelength 490 nm/515 nm. Panels C: panels A and B overlay for CTRL and **(*S*)-AuL1** treatment. Representative fields of three separate experiments are shown.

experimental section. As shown in Fig. 3, MDA-MB-231 cells treated with **(*S*)-AuL1** showed green fluorescence (panel B) that perfectly overlapped the blue fluorescence (panel A) from cell nuclei, which strongly indicate marked genomic DNA damage (panel C). In contrast, MDA-MB-231 cells exposed to the vehicle (DMSO, CTRL) did not show the green fluorescence (Fig. 2, panel B, CTRL), meaning that the nuclear DNA was undamaged (panels A and C, CTRL). The latter observations confirmed that the selective impact of **(*S*)-AuL1** on MDA-MB-231 breast cancer cell viability depends on the cell death triggered by the nuclear DNA damage, due to the inhibition of hTopoI.

Anti-inflammatory properties

The anti-inflammatory properties of the new series of synthesized enantiopure complexes were determined in murine macrophages RAW 264.7, measuring the NO production under bacterial lipopolysaccharide (LPS) stimulation by the means of the Griess reagent. A nonsteroidal anti-inflammatory drug (NSAID), *i.e.* indomethacin (Ind), was employed as the positive control. Two concentrations, 5 and 10 μM, chosen after testing the enantiopure pro-ligands and relative complexes for their cytotoxicity on the RAW264.7 murine macrophages *via* the MTT assay, were employed for the anti-inflammatory assay. The measurements were made after 24 hours of treatment. Ind was used at 5, 10 and 50 μM. As shown in Fig. 4, none of the assayed molecules produced a significant decrease of cell viability, with the exception of **(*R*)-AuL1**, **(*S*)-** and **(*R*)-AuL2** at 10 μM, which reduced the viability by about 55–45%.

Fig. 5 shows the results from the NO production measurements, where it is possible to see that none of the enantiopure pro-ligands **P1** and **P2** influenced the NO production under LPS stimulation.

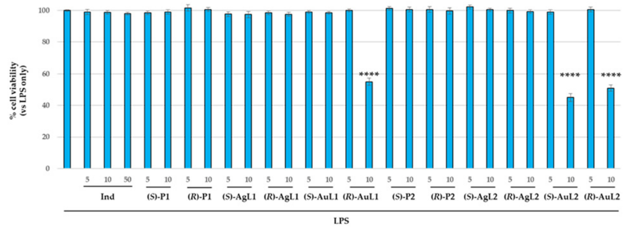

Fig. 4 MTT test was performed to evaluate the possible cytotoxic effects of enantiopure pro-ligands and complexes, used at the concentrations of 5 and 10 μM, and indomethacin (Ind), used as a reference molecule, at the concentrations of 5, 10 and 50 μM, on murine macrophages RAW 264.7. Columns ± SD represent the % of residual cell viability with respect to LPS-only treatment (1 μg mL^{-1}). Three different experiments were performed in triplicate. **** $p < 0.0001$, or not significant (n.s., not indicated), treated *vs.* LPS only.

Similar results were obtained from Ag-based complexes, whereas those bearing Au were found to be able to significantly decrease the induced NO production. Overall, **(*S*)-AuL1** was found the most active, in reducing the NO production dose-dependently, of about 33 and 57% at 5 and 10 μM, respectively. It is important to emphasize that its enantiomer, **(*R*)-AuL1**, not only produced a lesser effect against the NO production (about 18%) at 5 μM, but it was also cytotoxic at the concentration of 10 μM (Fig. 4), which made the evaluation of NO production at the higher concentration misrepresented and useless (Fig. 5, not determined, n.d.). The other complexes **(*S*)-** and **(*R*)-AuL2**, bearing two stereocenters and an additional 2-phenylethyl substituent on the NHC core that raises the lipophilicity, demonstrated a low activity in decreasing the NO production with respect to **(*S*)-AuL1**, for both equal to about 18%, respectively, at the concentration of 5 μM, and the configuration seems not to play any role. Furthermore, they were found both cytotoxic at 10 μM (Fig. 4 and 5, not determined, n.d.). Notably, the complex **(*S*)-AuL1** also exhibited a better activity than the reference molecule, Ind, which was able to reduce the NO stimulated production by

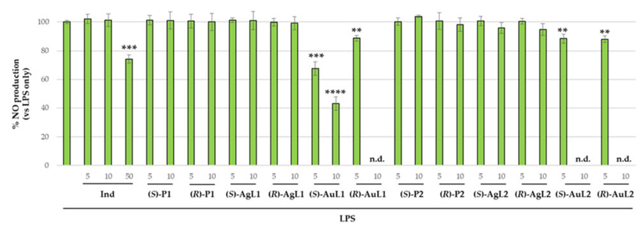

Fig. 5 Anti-inflammatory activity of the enantiopure complexes and pro-ligands, at the indicated concentrations expressed as μM (5 and 10) for 24 h, in terms of NO production in murine macrophages RAW 264.7 treated with LPS (1 μg mL^{-1}). Columns are the mean ± SD of three separated experiments, conducted in triplicate, and represent the % of NO production with respect to LPS-only treatment (first column). Indomethacin (Ind) was used as the reference compound. Columns ± SD are shown. ** $p > 0.01$, *** $p > 0.001$, **** $p < 0.0001$, or not significant (whether not indicated), treated *vs.* LPS only; n.d., not determined.

only about 26% at 50 μM, namely ten- and five-fold higher concentrations than those adopted for (*S*)-**AuL1** (Fig. 5). These outcomes suggest that only the complexes bearing gold inhibited the NO production in stimulated RAW 264.7 cells and that the configuration is absolutely responsible for the observed different activity in **L1** series. Finally, the increase of the lipophilicity (see (*S*)-**AuL1** *versus* (*S*)-**AuL2**) is inversely proportional to the observed ability in inhibiting iNOS and, consequently, decreasing the NO production in the adopted cell context, confirming that for the most active complex (*S*)-**AuL1**, the lipophilicity tuning, due to the difference of substituents on the NHC core, contribute to the inhibitory activity.[4] These outcomes are also in agreement with other published studies on structurally different iNOS inhibitors, even though little is still known about enantiopure inhibitors.[24,25] It is accepted that iNOS modulation represents an important key-point in medicinal chemistry, since its overexpression and/or deregulation are linked to the onset and progression of several chronic diseases, included cancer.[26] Additionally, drugs targeting iNOS may modulate its activity, as well as its expression, contributing to the varied amounts of NO production.[27] Thus, the expression of iNOS in murine macrophages RAW 264.7 was assessed by the means of immunofluorescence assays, and the obtained results are shown in Fig. 6.

Particularly, LPS-stimulated macrophages revealed, as expected, an enhanced iNOS expression (red fluorescence, Fig. 6, panel 2A) with respect to cells treated with only the vehicle (DMSO) that showed basal levels (Fig. 6, panel 1A). The co-treatment with the enantiopure complexes (*S*)-**AuL1** or (*S*)-**AuL2** at 5 μM resulted in a net diminution of the intracellular iNOS expression, as shown in Fig. 6, panels 4A and 5A, with respect to the LPS-treated cells (panel 2A), mostly for (*S*)-**AuL1** treatment. A similar behavior was found under ind co-treatment (Fig. 6, panel 3A), which was used at 50 μM (ten-fold higher than the concentration used for the complexes).

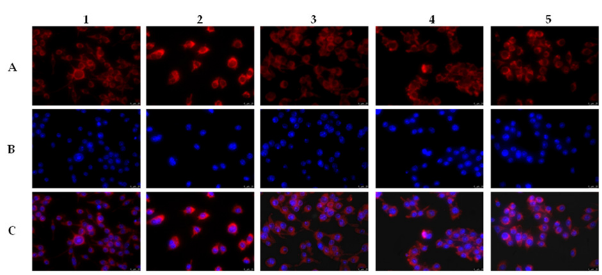

Fig. 6 Semi-quantitative evaluation of the iNOS expression in murine macrophages RAW 264.7 by immunofluorescence assays. 1: RAW 264.7 cells treated with only the vehicle (DMSO). 2: RAW 264.7 cells treated with LPS (1 μg mL^{-1}). 3: RAW 264.7 cells co-treated with LPS (1 μg mL^{-1}) and indomethacin (50 μM). 4 and 5: RAW 264.7 cells co-treated with LPS (1 μg mL^{-1}) and (*S*)-**AuL1** or (*S*)-**AuL2** (5 μM), respectively. Panels A, DAPI ($\lambda_{ex/em}$ = 350/460 nm); panels B, AlexaFluor®568 ($\lambda_{ex/em}$ = 644/665 nm); panels C, merge. Images were taken at 40×. Two independent experiments were performed, and representative fields are shown.

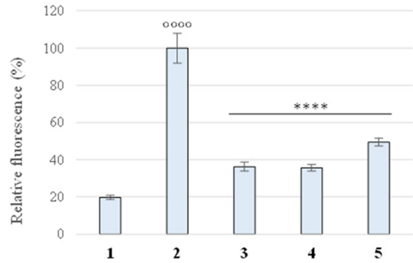

Fig. 7 Fluorescence quantification of iNOS expression, in RAW 264.7 cells, using ImageJ software; 1: vehicle (DMSO). 2: LPS (1 μg mL^{-1}). 3: LPS (1 μg mL^{-1}) + indomethacin (50 μM). 4: LPS (1 μg mL^{-1}) + (*S*)-**AuL1** (5 μM). 5: LPS (1 μg mL^{-1}) + (*S*)-**AuL2** (5 μM). Columns ± SD are shown. °°°° $p < 0.0001$ LPS only *vs.* CTRL, ****$p < 0.0001$, co-treated *vs.* 2 LPS only.

Overall, (*S*)-**AuL1** was found to be able to reduce iNOS expression with a similar potency to ind, as it is easily deducible observing the fluorescence quantification graphic in Fig. 7, but at a ten-fold lower concentration.

This feature is also strictly connected with the previously shown results on the great impact of (*S*)-**AuL1** on the viability of breast cancer cells, mostly for the highly aggressive and metastatic MDA-MB-231 cells. Indeed, the overexpression of iNOS is generally associated with poor outcomes in triple negative breast cancer (TNBC) patients;[28] thus, the development of molecules able to modulate iNOS activity and expression represents a current and promising strategy in the anticancer therapy.

Docking simulations

Molecular docking simulations (Fig. 8) identified specific and well-defined binding modes for all tested compounds within the active site region of human iNOS, in close proximity to the heme prosthetic group. All four ligands exhibited interactions characteristic of metallodrug–protein complexes, involving both coordination bonds with the Au(I) center and non-covalent contacts, including hydrogen bonding and π-stacking.

(*S*)-**AuL1** was found to establish a direct coordination between its gold atom and the carboxylate group of Glu371, a key residue at the entrance of the heme pocket. The coordinated chlorine atom of (*S*)-**AuL1** engaged in simultaneous interactions with the backbone amide nitrogen of Met368 and contributed to the stabilization of the complex. Furthermore, a π-stacking interaction was observed between a phenyl ring of the ligand and the porphyrin plane of the heme group, further anchoring the molecule in the binding pocket. (*R*)-**AuL1** adopted a binding conformation characterized by strong coordination of the gold atom to a carboxylate oxygen atom (Cox) of the heme group, while the chlorine atom simultaneously interacted with a second Cox group on the same porphyrin structure. A phenyl ring of the ligand established a coplanar π-stacking interaction with the heme, stabilizing the compound in a conformation reminiscent of known iNOS inhibitors.

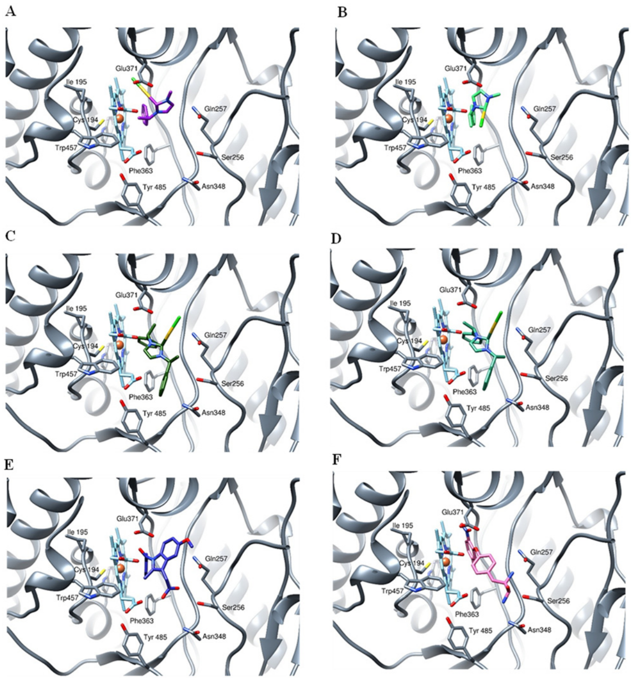

Fig. 8 Ligand binding modes resulting from docking simulations. The protein tertiary structure is shown as grey ribbons, with the heme group represented as cyan sticks. Ligands are depicted as colored sticks: panel A) **(*S*)-AuL1**; panel B) **(*R*)-AuL1**; panel C) **(*S*)-AuL2**; panel D) **(*R*)-AuL2**. The last two panels present the crystallographic poses of indomethacin (Ind, panel E) and *N*-(4-hydroxyphenyl)-2-naphthamide (YW0, panel F) for comparison.

(*S*)-AuL2 displayed a distinct binding pose in which the gold center coordinated the side chain of Gln257, while the chlorine atom formed a hydrogen bond with the hydroxyl group of Tyr367. The aromatic system of the ligand simultaneously engaged in dual π–π stacking interactions with both the heme prosthetic group and the aromatic ring of Tyr485, suggesting a favourable orientation for electronic delocalization and stabilization. **(*R*)-AuL2** shared the same interaction profile as **(*S*)-AuL2**, with the coordination of Au to Gln257, hydrogen bonding between the chlorine atom and Tyr367, and π-stacking with both heme and Tyr485. However, the spatial arrangement of the aromatic groups differed slightly, potentially contributing to minor variations in the calculated binding affinities.

The calculated binding energies and predicted inhibition constants (K_i) for all four complexes are summarized in Table 3. These results support the hypothesis that both the Au–protein coordination and the geometry of π-stacking with the heme and adjacent residues are critical determinants of binding affinity.

Table 3 Binding energies and affinities of the tested complexes to iNOS

	K_i (μM)	$E_{binding}$ (kcal per mole)
(*S*)-AuL1	2.3	−8.59
(*R*)-AuL1	2.24	−8.6
(*S*)-AuL2	0.55	−10.03
(*R*)-AuL2	0.33	−10.33

In AutoDock, the inhibition constant (K_i) is calculated from the estimated binding free energy (ΔG) of the ligand–receptor complex using the following thermodynamic relationship:

$$K_i = \exp[(\Delta G \times 1000)/(R \times T)]$$

where:

• ΔG is the predicted binding free energy (in kcal mol^{-1}), returned by AutoDock for the best-ranked pose.

• R is the universal gas constant (1.987 cal mol^{-1} K^{-1}).

• T is the temperature in Kelvin, typically set at 298.15 K (25 °C) by default in AutoDock.

Antioxidant activity. Cancer onset and development involve different aspects, as genetic mutations, environmental factors, lifestyle habits and so on, but the rise of reactive oxygen species (ROS) production during oxidative stress can worsen this condition, damaging biological macromolecules and enhancing mutations.[29] Besides, tumorigenesis can be promoted by chronic inflammation supported by macrophages and other immune cells that maintain high levels of inflammatory mediators.[26] Antioxidant agents can lower ROS generation but also regulate cytokine production and activity, reducing inflammation; thus, the antioxidant power of a molecule is an important feature that can be exploited for hampering the two above-mentioned and connected events that promote cancer cell proliferation and the invasion phenomena. Therefore, aiming at the evaluation of the ability of the new enantiopure complexes in inhibiting the ROS production, the RAW 264.7 murine macrophages were chosen as the cell model, and the dihydro-2′,7′-dichlorofluorescein diacetate (H_2DCF-DA) fluorescent probe was used for intracellular ROS detection. Particularly, RAW 264.7 cells were treated for the Griess assay, as described before, under the same experimental conditions. Indeed, LPS stimulation is able to induce the inflammatory cascades and, consequently, oxidative stress and the intracellular accumulation of ROS.[30] As a positive control, a powerful antioxidant compound, *i.e.* *N*-acetyl-cysteine (NAC), at 5×10^3, 10×10^3, and 20×10^3 μM concentrations that do not

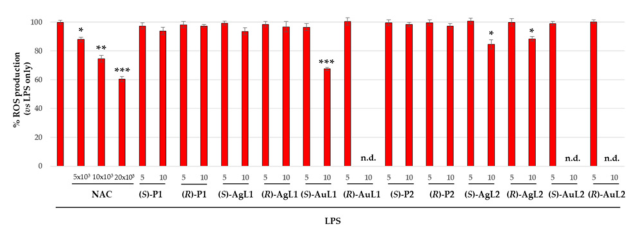

Fig. 9 Antioxidant activity expressed as percentage (%) of ROS production. The RAW 264.7 murine macrophages were treated with LPS for inducing ROS production. The enantiopure complexes and pro-ligands were used at the indicated concentrations (5 and 10 μM) whereas NAC (positive control) at 5×10^3, 10×10^3, and 20×10^3 μM. Columns ± SD are shown (three experiments, each in triplicate). $p < 0.05$, ** $p < 0.01$, *** $p < 0.001$, or not significant if not indicated, co-treated *vs.* LPS only. n.d., not determined.

hamper cell viability (about 98.7% of residual viability *vs.* LPS-treated cells, data not shown), was used. Pro-ligands were also tested. Fig. 9 shows the obtained outcomes, where it is possible to see that **(*S*)-AuL1** possessed the higher antioxidant activity. Indeed, at 10 μM concentration, it was able to reduce the ROS production of about the 32%. Its enantiomer, conversely, was not determined at 10 μM because of its cytotoxicity toward the adopted cells (see Fig. 4).

It is important to highlight that NAC exhibited a reduction in ROS levels of about 25 and 40% at 10×10^3 and 20×10^3 μM, respectively, which are 1000 and 2000-fold higher than the **(*S*)-AuL1** effective concentration (Fig. 9). Furthermore, a slight antioxidant activity was recorded for both the enantiopure complexes **(*S*)-AgL2** and **(*R*)-AgL2**, about 15 and 12% ROS reduction, respectively, whereas the pro-ligands were found inactive. Finally, complexes **(*S*)-AuL2** and **(*R*)-AuL2** did not exert any antioxidant activity at the lower dosage (Fig. 9) and were found cytotoxic at the highest concentration (Fig. 4).

Summing up, **(*S*)-AuL1** is the best antioxidant and anti-inflammatory complex, and was also found as the best and selective anticancer candidate. Meanwhile, its enantiomer **(*R*)-AuL1** demonstrated a lesser activity in all the described experiments and also a dose dependent cytotoxicity toward the adopted cell models, both cancerous and normal.

Conclusions

In this paper, we reported the synthesis of a new series of enantiopure NHC–silver(I) and NHC–gold(I) complexes and disclosed some of their biological activities, such as anticancer, anti-inflammatory and antioxidant properties. We also individuated two important enzymes, namely hTopoI and iNOS, modulated by the most active complex and related to the above-mentioned activities. The reported results indicate that the gold(I)-based complexes are the most active and that the configuration and chemical substituents are fundamental for the modulatory properties exerted toward these two enzymes. Most interestingly, the stronger inhibitory activity exerted by **(*R*)-AuL1** toward hTopoI with respect to **(*S*)-AuL1**, which is, instead, the best and more selective anticancer candidate, could be one of the main causes involved in the high cytotoxicity of **(*R*)-AuL1** toward the normal breast cells used in these assays. **(*S*)-AuL1** was also found to be the best iNOS inhibitor and antioxidant complex, and also the less cytotoxic toward the RAW 264.7 cells. Considering that there are only few literature reports in the field of NHC–gold and NHC–silver complexes, the present outcomes contribute to widen the knowledge about the design of more potent, selective and safer complexes to be further developed for the treatment of multifactorial diseases.

Experimental section

All reagents were purchased from Merck Italy (Milan, Italy) and TCI Chemicals (Zwijndrecht, Belgium) and used without any purification. All solvents were bought from Carlo Erba Reagents srl (Milano, Italy) and were distilled over appropriate drying agents under nitrogen before use. The synthesis of silver(I) and gold(I) complexes was carried out under a nitrogen atmosphere by using Schlenk techniques in the dark. The glassware used was dried in an oven at 120 °C overnight. Deuterated solvents were dried on molecular sieves. ^{1}H and ^{13}C nuclear magnetic resonance spectra (NMR) were acquired on a Bruker Avance 300 spectrometer (300 MHz for ^{1}H; 75 MHz for ^{13}C), a Bruker AVANCE 400 spectrometer (400 MHz for ^{1}H; 100 MHz for ^{13}C) and a Bruker AVANCE 600 spectrometer (600.13 MHz for ^{1}H, 150.90 MHz for ^{13}C), operating at 298 K. NMR samples were prepared by dissolving about 15 mg of the compound in 0.5 mL of deuterated solvent (Eurisotop Cambridge Isotope Laboratories, Cambridge, UK). The chemical shifts of ^{1}H-NMR and ^{13}C-NMR spectra are referenced using the residual proton impurities of the deuterated solvents. ^{1}H-NMR was reported relative to $CDCl_3$ δ 7.26 ppm. ^{13}C-NMR was reported relative to $CDCl_3$ δ 77.16 ppm. The spectral multiplicities are indicated as follows: singlet (s), doublet (d), triplet (t), multiplet (m), and broad (br). MALDI-MS mass spectra were obtained using a Bruker SolariX XR Fourier transform ion cyclotron resonance mass spectrometer (Bruker Daltonik GmbH, Bremen, Germany) with a 7 T refrigerated actively shielded superconducting magnet (Bruker Biospin, Wissembourg, France). A MALDI ion source (Bruker Daltonik GmbH, Bremen, Germany) was used for the samples in positive ion mode. The mass range was set to m/z 200–3000. The laser power was 28% and 22 laser shots were utilized for each scan. The mass spectra were calibrated externally using a mix of peptide clusters in MALDI ionization positive ion mode. Ultraviolet-visible (UV-vis) measurements were performed with an Agilent Varian Cary 50 spectrophotometer (Agilent Technologies Inc., Santa Clara, California, USA). Optical rotations were measured on a digital polarimeter (JASCO P-2000) at a concentration of C = 0.50. A sodium lamp (λ = 589 nm) was used as a light source.

Chemistry

Complexes **(*S*)-AgL2**/**(*S*)-AuL2** (ref. 15) and **(*R*)-AgL2**/**(*R*)-AuL2** were synthesized according to literature procedures,[15] with slight modifications.

Synthesis of proligands (*S*)-P1/(*R*)-P1. To a stirred solution of (*S*)- or (*R*)-α-methylbenzylamine (1.00 g, 8.25 mmol) in anhydrous methanol (10 mL) at 0 °C, 37% aqueous formaldehyde was added (0.62 mL, 8.25 mmol). The mixture was stirred until complete formation of a white solid (10–15 min). Then, ammonium carbonate (0.40 g, 4.13 mmol) and 40% aqueous glyoxal (0.94 mL, 8.25 mmol) were subsequently added and the mixture was stirred at room temperature overnight. Then, the reaction mixture was quenched with brine (10 mL) and washed with hexane (20 mL). Methanol was evaporated from the aqueous phase and then extracted with chloroform (3 × 10 mL). The organic layer was dried over anhydrous magnesium sulphate, filtered, and evaporated to dryness to obtain brownish oil.

(S)-1-(1-Phenylethyl)-1H-imidazole (0.596 g, 42%). **^{1}H-NMR (600 MHz, $CDCl_3$, ppm) δ:** 7.58 (1H, s, NC*H*N), 7.33 (3H, m, Ar–*H*), 7.16 (2H, d, *J* = 7.2 Hz, Ar–*H*), 7.06 (1H, s, NC*H*CHN), 6.92 (1H, s, NCHC*H*N), 5.33 (1H, q, *J* = 7.2 Hz, C*H*CH_3), 1.85 (3H, d, *J* = 7.2 Hz, CHCH_3).

^{13}C-NMR (150 MHz, $CDCl_3$, ppm) δ: 141.1, 135.6, 128.8, 128.4, 127.6, 125.5, 117.5, 56.1, 21.6.

(R)-1-(1-Phenylethyl)-1H-imidazole (0.738 g, 52%). **^{1}H-NMR (600 MHz, $CDCl_3$, ppm) δ:** 7.58 (1H, s, NC*H*N), 7.33 (3H, m, Ar–*H*), 7.15 (2H, d, *J* = 7.2 Hz, Ar–*H*), 7.06 (1H, s, NC*H*CHN), 6.92 (1H, s, NCHC*H*N), 5.33 (1H, q, *J* = 7.2 Hz, C*H*CH_3), 1.84 (3H, d, *J* = 7.2 Hz, CHCH_3).

^{13}C-NMR (150 MHz, $CDCl_3$, ppm) δ: 141.1, 135.6, 128.8, 128.4, 127.6, 125.5, 117.5, 56.1, 21.6.

The resulting crude intermediate (*S*/*R*)-1-(1-phenylethyl)-1*H*-imidazole (0.500 g, 2.91 mmol) was dissolved in acetonitrile (10 mL), and iodomethane (1.27 mL, 20.4 mmol) was added. The resulting mixture was stirred at reflux for 5 hours, then brought to room temperature and evaporated to dryness. Precipitation from acetone gave resulting salts **(*S*)-P1**/**(*R*)-P1** as white solids.

*(S)-3-Methyl-1-(1-phenylethyl)-1H-imidazol-3-ium iodide (**(S)-P1**, 0.874 g, 96%).* **^{1}H-NMR (600 MHz, $CDCl_3$, ppm) δ:** 10.0 (1H, s, NC*H*N), 7.48 (1H, s, NC*H*CHN), 7.42 (2H, d, *J* = 7.8 Hz Ar–*H*), 7.38–7.34 (3H, overlapping signals, Ar–*H*), 7.26 (1H, br s, NCHC*H*N), 5.85 (1H, q, *J* = 7.2 Hz, C*H*CH_3), 4.08 (3H, s, NCH_3), 2.00 (3H, d, *J* = 7.2 Hz, CHCH_3).

^{13}C-NMR (150 MHz, $CDCl_3$, ppm) δ: 137.7, 136.1, 129.5, 127.0, 123.9, 120.9, 60.1, 37.3, 21.5.

(MALDI-ICR FTMS) *m*/*z*: HRMS calcd for $C_{12}H_{15}N_2^+$: 187.1230, found: 187.1225.

*(R)-3-Methyl-1-(1-phenylethyl)-1H-imidazol-3-ium iodide (**(R)-P1**, 0.847 g, 93%).* **^{1}H-NMR (600 MHz, $CDCl_3$, ppm) δ:** 10.0 (1H, s, NC*H*N), 7.48 (1H, s, NC*H*CHN), 7.42 (2H, d, *J* = 7.8 Hz Ar–*H*), 7.38–7.34 (3H, overlapping signals, Ar–*H*), 7.26 (1H, br s, NCHC*H*N), 5.85 (1H, q, *J* = 7.2 Hz, C*H*CH_3), 4.08 (3H, s, NCH_3), 2.00 (3H, d, *J* = 7.2 Hz, CHCH_3).

^{13}C-NMR (150 MHz, $CDCl_3$, ppm) δ: 137.7, 136.2, 129.5, 127.1, 123.8, 120.8, 60.1, 37.3, 21.5.

(MALDI-ICR FTMS) *m*/*z*: HRMS calcd for $C_{12}H_{15}N_2^+$: 187.1230, found: 187.1223.

Synthesis of proligands (*S*)-P2/(*R*)-P2. Symmetric chiral proligand imidazolium salts **(*S*)-P2**/**(*R*)-P2** were synthesized according to literature procedures.[15]

To a stirred solution of (*S*)- or (*R*)-α-methylbenzylamine (2.02 g, 16.6 mmol) in toluene (18 mL), paraformaldehyde (0.50 g, 16.6 mmol) was added. After 30 min, the mixture was cooled to 0 °C and another equivalent of (*S*)- or (*R*)-α-methylbenzylamine (2.02 g, 16.6 mmol) was added, followed by 3 M HCl (4.97 mL, 16.6 mmol). After 15 min, the reaction was brought to room temperature, and glyoxal (1.89 mL, 16.6 mmol, 40% aqueous solution) was slowly added. The mixture was stirred for 12 h at 40 °C and then cooled to room temperature. The reaction was quenched with 2 mL of sat. solution of Na_2CO_3, then 10 mL of H_2O and 10 mL of Et_2O were added, the phases separated and the aqueous layer was washed with CH_2Cl_2 (3 × 10 mL). The organic phases were collected and dried over $MgSO_4$, concentrated *in vacuo*. The residue was triturated with Et_2O to give 1,3-bis((*S*)- or (*R*)-1′-phenylethyl)imidazolium chloride (**(*S*)-P2**/**(*R*)-P2**) as off-white powders.

*1,3-Bis((S)-1′-phenylethyl)imidazolium chloride (**(S)-P2**, 3.58 g, 69%)*[15]. NMR and HRMS characterization results were consistent with what already reported in the literature.

*1,3-Bis((R)-1′-phenylethyl)imidazolium chloride (**(R)-P2**, 3.17 g, 61%).* **^{1}H NMR (600 MHz, $CDCl_3$, ppm) δ:** 11.59 (1H, s, NC*H*N), 7.45 (2H, br d, *J* 7.5 Hz, Ar–*H*), 7.40–7.35 (6H, overlapping, Ar–*H*), 7.04 (2H, s, NC*H*C*H*N), 6.05 (2H, q, *J* 7.2 Hz, NC*H*CH_3), 2.03 (6H, d, *J* 7.2 Hz, NCHCH_3).

^{13}C NMR (150 MHz, $CDCl_3$, ppm) δ: 137.8, 137.3, 129.4, 127.1, 119.9, 59.9, 21.2.

(MALDI-ICR FTMS) *m*/*z*: HRMS calculated for $C_{19}H_{21}N_2^+$: 277.3905, found: 277.3901.

Synthesis of silver complexes (*S*)-AgL1/(*R*)-AgL1. To a stirred solution of chiral proligand **(*S*)-P1**/**(*R*)-P1** (0.404 g, 1.29 mmol) in dry dichloromethane (43 mL), under an inert atmosphere, silver nitrate (0.262 g, 1.29 mmol) was added. The resulting suspension was stirred at reflux for 2 hours, then potassium carbonate (1.78 g, 12.9 mmol) was added. The reaction mixture was refluxed overnight, then cooled to room temperature and filtered through a celite plug. The solvent was evaporated to complete dryness, and the resulting powder was washed with diethyl ether (3 × 10 mL) to obtain the off-white powders of complexes **(*S*)-AgL1**/**(*R*)-AgL1**.

*(S)-3-Methyl-1-(1-phenylethyl)-1H-imidazol-3-ium silver(I) iodide (**(S)-AgL1**, 0.440 g, 81%).* **^{1}H NMR (600 MHz, $CDCl_3$, ppm) δ:** 7.32–7.28 (5H, overlapping signals, Ar–*H*), 6.97 (1H, d, *J* = 1.2 Hz, NC*H*CHN), 6.93 (1H, d, *J* = 1.8 Hz, NCHC*H*N), 5.89 (1H, q, *J* = 7.2 Hz, C*H*CH_3), 3.82 (3H, s, NCH_3), 1.82 (3H, d, *J* = 7.2 Hz, CHCH_3).

^{13}C-NMR (150 MHz, $CDCl_3$, ppm) δ: 183.2, 140.6, 128.8, 128.1, 126.6, 122.3, 118.6, 60.0, 39.0, 21.6.

(MALDI-ICR FTMS) *m*/*z*: HRMS calculated for $C_{12}H_{15}AgIN_2^+$: 422.0381, found: 422.0379.

Elemental analysis: calculated for $C_{12}H_{14}AgIN_2$ C, 34.23; H, 3.35; Ag, 25.62; I, 30.14; N, 6.65; found C, 34.12; H, 3.40; Ag, 25.68; I, 30.20; N, 6.70.

*(R)-3-Methyl-1-(1-phenylethyl)-1H-imidazol-3-ium silver(I) iodide (**(R)-AgL1**, 0.430 g, 79%).* **^{1}H NMR (600 MHz, $CDCl_3$, ppm) δ:** 7.32–7.28 (5H, overlapping signals, Ar–*H*), 6.97 (1H, d, *J* = 1.2 Hz, NC*H*CHN), 6.92 (1H, d, *J* = 1.8 Hz, NCHC*H*N), 5.89 (1H, q, *J* = 7.1 Hz, C*H*CH_3), 3.82 (3H, s, NCH_3), 1.81 (3H, d, *J* = 7.2 Hz, CHCH_3).

^{13}C-NMR (150 MHz, $CDCl_3$, ppm) δ: 183.2, 140.6, 128.8, 128.1, 126.6, 122.3, 118.6, 60.0, 39.0, 21.6.

(MALDI-ICR FTMS) *m*/*z*: HRMS calculated for $C_{12}H_{15}AgIN_2^+$: 422.0381, found: 422.0384.

Elemental analysis: calculated for $C_{12}H_{14}AgIN_2$ C, 34.23; H, 3.35; Ag, 25.62; I, 30.14; N, 6.65; found C, 34.25; H, 3.36; Ag, 25.65; I, 30.11; N, 6.68.

Synthesis of gold complexes (*S*)-AuL1/(*R*)-AuL1. Silver complexes **(*S*)-AgL1**/**(*R*)-AgL1** (0.204 g, 0.484 mmol) were dissolved in dry dichloromethane (24 mL) under an inert atmosphere; $(CH_3)_2SAuCl$ (0.142 g, 0.484 mmol) was added, and the resulting solution was stirred at room temperature overnight. Then, the reaction mixture was cooled to room temperature and filtered through a celite plug. The solvent was evaporated to complete dryness, and the resulting powder was washed with diethyl ether (3 × 10 mL), obtaining the off-yellow powders of complexes **(*S*)-AuL1**/**(*R*)-AuL1**.

*(S)-3-Methyl-1-(1-phenylethyl)-1H-imidazol-3-ium gold(I) chloride ((**S**)-AuL1, 0.183 g, 90%).* **^{1}H NMR (600 MHz, $CDCl_3$, ppm) *δ*:** 7.36–7.31 (5H, overlapping signals, Ar–$\underline{H}$), 6.91 (1H, d, *J* = 1.8 Hz, NC$\underline{H}$CHN), 6.85 (1H, d, *J* = 1.8 Hz, NCHC$\underline{H}$N), 6.14 (1H, q, *J* = 7.2 Hz, C$\underline{H}CH_3$), 3.82 (3H, s, NC$\underline{H_3}$), 1.84 (3H, d, *J* = 7.2 Hz, CHC$\underline{H_3}$).

^{13}C-NMR (150 MHz, $CDCl_3$, ppm) *δ*: 170.8, 138.2, 129.0, 128.6, 126.8, 122.2, 117.8, 59.8, 38.3, 20.7.

(MALDI-ICR FTMS) *m*/*z*: HRMS calculated for $C_{12}H_{15}AuClN_2^+$: 419.6820, found: 419.6818.

Elemental analysis: calculated for $C_{12}H_{14}AuClN_2$ C, 34.43; H, 3.37; Au, 47.05; Cl, 8.47; N, 6.69; found C, 34.50; H, 3.25; Au, 47.03; Cl, 8.41; N, 6.73.

*(R)-3-Methyl-1-(1-phenylethyl)-1H-imidazol-3-ium gold(I) chloride ((**R**)-AuL1, 0.183 g, 90%).* **^{1}H NMR (600 MHz, $CDCl_3$, ppm) *δ*:** 7.37–7.32 (5H, overlapping signals, Ar–$\underline{H}$), 6.87 (1H, d, *J* = 1.8 Hz, NC$\underline{H}$CHN), 6.85 (1H, d, *J* = 1.8 Hz, NCHC$\underline{H}$N), 6.13 (1H, q, *J* = 7.2 Hz, C$\underline{H}CH_3$), 3.83 (3H, s, NC$\underline{H_3}$), 1.84 (3H, d, *J* = 7.2 Hz, CHC$\underline{H_3}$).

^{13}C-NMR (150 MHz, $CDCl_3$, ppm) *δ*: 169.9, 138.2, 128.0, 127.6, 125.8, 121.1, 116.8, 58.8, 37.3, 19.7.

(MALDI-ICR FTMS) *m*/*z*: HRMS calculated for $C_{12}H_{15}AuClN_2^+$: 419.6820, found: 419.6819.

Elemental analysis: calculated for $C_{12}H_{14}AuClN_2$ C, 34.43; H, 3.37; Au, 47.05; Cl, 8.47; N, 6.69; found C, 34.37; H, 3.34; Au, 47.09; Cl, 8.51; N, 6.72.

Synthesis of silver complexes (*S*)-AgL2/(*R*)-AgL2. Symmetric chiral silver complexes **(*S*)-AgL2**/**(*R*)-AgL2** were synthesized according to literature procedures.[15]

To a stirred solution of chiral proligand **(*S*)-P2**/**(*R*)-P2** (0.500 g, 1.60 mmol) in dry dichloromethane (53 mL), under inert atmosphere, 4 Å molecular sieves were added, followed by silver oxide (0.444 g, 1.92 mmol). The suspension was stirred at reflux overnight, then cooled to room temperature and filtered through a celite plug. The solvent was evaporated to complete dryness, and the resulting powder was washed with hexane (3 × 10 mL) to obtain the off-white powders of complexes **(*S*)-AgL2**/**(*R*)-AgL2**.

*1,3-Bis((S)-1′-phenylethyl)imidazolium silver(I) chloride ((**S**)-AgL2, 0.463 g, 69%)*[15]. NMR and HRMS characterization results were consistent with what already reported in the literature.

*1,3-Bis((R)-1′-phenylethyl)imidazolium silver(I) chloride ((**R**)-AgL2, 0.335 g, 50%).* **^{1}H NMR (600 MHz, $CDCl_3$, ppm) *δ*:** 7.37–7.26 (10H, overlapping signals, Ar–$\underline{H}$), 6.92 (2H, s, NC$\underline{H}$C$\underline{H}$N), 5.76 (2H, q, *J* = 7.0 Hz, C$\underline{H}CH_3$), 1.84 (6H, d, *J* = 7.2 Hz, CHC$\underline{H_3}$).

^{13}C-NMR (150 MHz, $CDCl_3$, ppm) *δ*: 139.7, 129.1, 128.6, 126.6, 118.7, 61.0, 21.4.

(MALDI-ICR FTMS) *m*/*z*: HRMS calculated for $C_{19}H_{22}AgClN_2^+$: 421.7167, found: 421.7168.

Elemental analysis: calculated for $C_{19}H_{20}AgClN_2$ C, 54.37; H, 4.80; Ag, 25.70; Cl, 8.45; N, 6.67; found C, 54.33; H, 4.75; Ag, 25.65; Cl, 8.41; N, 6.71.

Synthesis of gold complexes (*S*)-AuL2/(*R*)-AuL2. Symmetric chiral silver complexes **(*S*)-AuL2**/**(*R*)-AuL2** were synthesized according to literature procedures.[15]

Silver complexes **(*S*)-AgL2**/**(*R*)-AgL2** (0.150 g, 0.317 mmol) were dissolved in dry dichloromethane (18 mL) under an inert atmosphere; $(CH_3)_2SAuCl$ (0.105 g, 0.317 mmol) was added, and the resulting mixture was stirred at room temperature overnight. After completion, the reaction mixture was cooled to room temperature and filtered through a celite plug. The solvent was evaporated to complete dryness, and the resulting powder was washed with hexane (3 × 10 mL) to obtain the off-yellow powders of complexes **(*S*)-AuL2**/**(*R*)-AuL2**.

*1,3-Bis((S)-1′-phenylethyl)imidazolium gold(I) chloride ((**S**)-AuL2, 0.077 g, 48%)*[15]. NMR and HRMS characterization was consistent with the previously reported literature.

*1,3-Bis((R)-1′-phenylethyl)imidazolium gold(I) chloride ((**R**)-AuL2, 0.089 g, 55%).* **^{1}H NMR (600 MHz, $CDCl_3$, ppm) *δ*:** 7.37–7.34 (10H, overlapping signals, Ar–$\underline{H}$), 6.82 (2H, s, NC$\underline{H}$C$\underline{H}$N), 6.17 (2H, q, *J* = 7.2 Hz, C$\underline{H}CH_3$), 1.84 (6H, d, *J* = 7.1 Hz, CHC$\underline{H_3}$).

^{13}C-NMR (150 MHz, $CDCl_3$, ppm) *δ*: 170.0, 139.2, 129.0, 128.6, 126.8, 118.1, 60.1, 20.8.

(MALDI-ICR FTMS) *m*/*z*: HRMS calculated for $C_{19}H_{22}AuClN_2^+$: 510.8150, found: 510.8148.

Elemental analysis: calculated for $C_{19}H_{20}AuClN_2$ C, 44.85; H, 3.96; Au, 38.71; Cl, 6.97; N, 5.51; found C, 44.79; H, 3.99; Au, 38.67; Cl, 6.97; N, 5.49.

Biology

Cell cultures. All the cells in the present study were obtained from American Type Culture Collection (ATCC, Manassas, VA, USA). Human breast cancer cells MCF-7 and MDA-MB-231 were maintained in Dulbecco's Modified Eagle Medium/Nutrient Mixture F12 Ham (DMEM/F12), added with 5% fetal bovine serum (FBS), 1% L-glutamine and 100 units per mL of penicillin/streptomycin. Human mammary epithelial cell line MCF-10A was maintained in a DMEM/F12 medium, added with 5% horse serum (HS), 100 units per mL of penicillin/streptomycin, 0.5 mg mL^{-1} hydrocortisone, 0.02 μg mL^{-1} human epidermal growth factor (EGF), 10 μg mL^{-1} insulin and 0.1 mg mL^{-1} cholera enterotoxin. The murine macrophages RAW 264.7 were cultured in Dulbecco's Modified Eagle's Medium (DMEM) high glucose (4.5 g L^{-1}), added with 10% fetal bovine serum (FBS), 1% L-glutamine and 100 units per mL of penicillin/streptomycin. Cells were kept at the temperature of 37 °C in a humidified atmosphere containing 5% CO_2.

MTT assay

The 3-(4,5-dimethylthiazol-2-y1)-2,5-diphenyltetrazolium bromide (MTT, Sigma-Aldrich, Milan, Italy) assay was used for cell viability determination, as already published.[31] Cells were seeded on 48 well plates, and then incubated for 24 h (for the anti-inflammatory/antioxidant activity studies) or 72 h (for the anticancer activity) with different concentrations of the tested compounds (dissolved in DMSO). The IC_{50} values, ± standard deviation (SD), were calculated from the percent (%) of control using the software GraphPad Prism 10 (GraphPad Software, La Jolla, CA, USA). For graphics, columns ± standard deviation (SD) represent the % of residual cell viability *vs.* the experimental control. Data are representative of three independent experiments performed in triplicate.

Human topoisomerase I relaxation assay

Human topoisomerase I (hTopo I) relaxation assays were performed, as already described (**https://doi.org/10.1016/j.ejmech.2024.116757**), using 2 units of the recombinant hTopo I and 0.25 μg of supercoiled plasmid pHOT1, as substrates (TopoGEN, Port Orange, FL, USA). The tested complexes, dissolved in DMSO, were used at the indicated concentrations. The mixture was incubated for 1 h at 37 °C, then loaded onto an 1% agarose gel made with 1× TAE buffer without ethidium bromide (EB). After the run, the gel was stained with EB (0.5 mg mL^{-1} in 1× TAE buffer) for 30 min, then washed with distilled water thrice for 5 min and visualized using a UV transilluminator.

TUNEL assay

TUNEL assay was used for nuclear DNA damage, according to the manufacturer instructions (One-step TUNEL Assay Kit (Green, FITC), MBS2567761, MyBioSource, Inc., San Diego, CA 92195-3308 USA). Briefly, cells were grown on glass cover slips, treated with **(*S*)-AuL1** at 1 μM (in DMSO), then PBS washed thrice and methanol-fixed (−20 °C, 15 min). The enzyme was added and incubated for 35 minutes at 37 °C, protected from light. Next, they were counterstained using a DAPI solution (0.2 mg mL^{-1}, 10 min, room temperature). After washing three times with cold PBS, one drop of mounting solution was added and cells were observed and imaged using a fluorescence microscope (Leica DM6000; 20× magnification) with excitation/emission wavelength maxima of 490 nm/515 nm (CFTM488A) or 350 nm/460 nm (DAPI). Representative fields of three independent experiments are shown.

Anti-inflammatory and antioxidant activity

The anti-inflammatory and the antioxidant activities in terms of NO and ROS production, respectively, were determined on LPS stimulated RAW 264.7 murine macrophages.[32] In detail, cells were plated on 48 multi-wells in a full medium, and after 24 hours, they were treated with the tested molecules (in DMSO), at the indicated concentrations, in a medium containing 1% of FBS, and lipopolysaccharide (LPS, Sigma Aldrich, Milan, Italy), at 1 μg mL^{-1}, was used to induce NO production and oxidative stress. After 24 h, the cell medium was harvested and mixed with the Griess reagent (1 : 1 ratio), then left under agitation for 30 min, at room temperature. The absorbance was measured by a multiplate reader, at 540 nm, and used for calculating the % of NO production compared to the control. For the antioxidant assays, after medium removal, cells were PBS-washed, added with 2′,7′-dichlorofluorescein diacetate (H_2DCFDA, 25 μM) and incubated (40 min, 37 °C, 5% CO_2). Then, cells were PBS-washed again and the fluorescence was quantified using a multiplate reader (λ_{ex} = 485 nm, λ_{em} = 535 nm). The ROS production *vs.* LPS, expressed as percentage (%), was calculated using the following formula:

$$\text{ROS } vs.\text{ LPS } (\%) = \frac{F_{\text{Sample}}}{F_{\text{LPS}}} \times 100$$

where F_{LPS} represents the mean fluorescence obtained for the LPS alone treatment and F_{sample} represents the mean fluorescence obtained for the co-treatment with LPS + tested compound.

Immunofluorescence studies

For the immunofluorescence (IF) studies, cells were grown on glass cover slips in a full medium, then treated with the complexes or indomethacin at the indicated concentrations (dissolved in DMSO), in a medium containing 1% of FBS for 24 h. Next, cells were PBS-washed, fixed with cold methanol (15 min, −20 °C) and incubated overnight (4 °C) with the anti-iNOS, (1 : 100, diluted in BSA 2%, Santa Cruz Biotechnology Inc., CA, USA), as described.[33] Alexa Fluor®568 conjugate goat-anti-mouse (1 : 500 diluted in BSA 2%, Thermo Fisher Scientific, MA, USA) was used as the secondary antibody. Nuclei were stained with 0.2 μg mL^{-1} of DAPI (10 min, Sigma Aldrich, Milan, Italy). Cells were visualized using a fluorescence microscope (Leica DM 6000) and LAS-X software (version 3.5.7.23225) was employed to acquire the images. Fluorescence quantification was done with Image J software (version 1.54d).

Docking studies. The crystallographic structure of human inducible nitric oxide synthase (iNOS) was retrieved from the Protein Data Bank [PDB ID: 4UX6].[34] The molecular structures of **(*S*)-AuL1**, **(*R*)-AuL1**, **(*S*)-AuL2** and **(*R*)-AuL2** were drawn and energy-minimized using MarvinSketch (ChemAxon, Budapest, HU). Docking simulations were performed with AutoDock v.4.2.2 using a blind docking protocol previously adopted by our group.[35] All ligands were considered fully flexible, while the receptor was kept rigid to reduce computational load. Preparation of both protein and ligands was carried out using AutoDock Tools (ADT), assigning Gasteiger charges and adding polar hydrogens.[36]

We adopted a protocol that was previously widely used by our group, some examples are described in ref. 37. Docking grids were centered on the whole protein to identify the most likely binding pockets. A grid box of 126 × 126 × 126 points with a spacing of 0.375 Å was used. Docking poses were clustered using a root mean square deviation (RMSD) cutoff of 2.0 Å. The best binding mode for each compound was selected from the lowest energy conformation within the most populated cluster. Images of the ligand–protein interactions were generated with UCSF Chimera.[38]

Data analysis

All the experiments were repeated three times, each in triplicate and the results were expressed as mean ± standard deviation (SD). Differences were determined by one-way analysis of variance (ANOVA), followed by Dunnett's multiple comparison test, performed using GraphPad Prism 10. Differences were considered significant at $p < 0.05$.

Conflicts of interest

The authors declare that they have no personal relationships that could have appeared to influence the work reported in this paper.

Data availability

Supplementary information: supplementary information (SI) reporting NMR characterization of the compounds is available. See DOI: **https://doi.org/10.1039/D5MD00651A**.

The data supporting this article have been included as part of the SI.

Acknowledgements

This work was supported by the Italian Ministry of Health (Ricerca Corrente) to Camillo Rosano, by PRIN 2022 PNRR, Code P20222BLAZ—Enhanced pharmacological activity of noble metal carbene-N-heterocyclic complexes by oligopeptide counterion (CUP MASTER: D53D23016900001)—and PRIN 2022, Code 2022HARH5W—HyMTA (Hybrid Multi-Target Agents) Synthesis and biological evaluation of chimeric hybrid molecules containing NHC-metal complexes and carbazole moieties, as innovative multi-target anticancer and antiviral agents (CUP MASTER: C53D23004490001). Mr Antonio Danubio is acknowledged for valuable experimental work.

References

1 N. Senkuttuvan, B. Komarasamy, R. Krishnamoorthy, S. Sarkar, S. Dhanasekaran and P. Anaikutti, *RSC Adv.*, 2024, **14**, 33429–33448.
2 L. Song, M. Pan, R. Zhao, J. Deng and Y. Wu, *J. Controlled Release*, 2020, **324**, 156–171.
3 C. Fliedel, A. Labande, E. Manoury and R. Poli, *Coord. Chem. Rev.*, 2019, **394**, 65–103.
4 M. Marra, A. Mariconda, D. Iacopetta, J. Ceramella, A. D'Amato, C. Rosano, K. Tkachenko, M. Pellegrino, S. Aquaro, M. S. Sinicropi and P. Longo, *Molecules*, 2024, **29**, 5262.
5 T. J. Siciliano, M. C. Deblock, K. M. Hindi, S. Durmus, M. J. Panzner, C. A. Tessier and W. J. Youngs, *J. Organomet. Chem.*, 2011, **696**, 1066–1071.
6 S. J. Berners-Price and A. Filipovska, *Metallomics*, 2011, **3**, 863–873.
7 S. A. Patil, S. A. Patil, R. Patil, R. S. Keri, S. Budagumpi, G. R. Balakrishna and M. Tacke, *Future Med. Chem.*, 2015, **7**, 1305–1333.
8 Y.-F. Zhang, Y.-K. Yin, H. Zhang and Y.-F. Han, *Coord. Chem. Rev.*, 2024, **514**, 215941.
9 I. Ott, *Coord. Chem. Rev.*, 2009, **253**, 1670–1681.
10 A. Mariconda, M. Sirignano, C. Costabile and P. Longo, *Mol. Catal.*, 2020, **480**, 110570.
11 C. Saturnino, I. Barone, D. Iacopetta, A. Mariconda, M. S. Sinicropi, C. Rosano, A. Campana, S. Catalano, P. Longo and S. Andò, *Future Med. Chem.*, 2016, **8**, 2213–2229.
12 M. Napoli, C. Saturnino, E. I. Cianciulli, M. Varcamonti, A. Zanfardino, G. Tommonaro and P. Longo, *J. Organomet. Chem.*, 2013, **725**, 46–53.
13 M. Sirignano, A. D'Amato, C. Costabile, A. Mariconda, A. Crispini, F. Scarpelli and P. Longo, *Front. Chem.*, 2023, **11**, 1260726.
14 A. P. da Costa, M. Sanaú, E. Peris and B. Royo, *Dalton Trans.*, 2009, 6960–6966.
15 G. A. Price, A. K. Brisdon, S. Randall, E. Lewis, D. M. Whittaker, R. G. Pritchard, C. A. Muryn, K. R. Flower and P. Quayle, *J. Organomet. Chem.*, 2017, **846**, 251–262.
16 E. V. Semenova, E. V. Belova, A. V. Sulimov and V. B. Sulimov, *Chirality*, 2024, **36**, e23712.
17 P. O. Wagers, M. J. Panzner, M. R. Southerland, M. A. DeBord, M. C. Deblock, C. A. Tessier, C. L. Cannon and W. J. Youngs, in *N-Heterocyclic Carbenes: From Laboratory Curiosities to Efficient Synthetic Tools*, ed. S. Diez-Gonzalez, The Royal Society of Chemistry, 2016, pp. 567–595.
18 A. Chimento, C. Saturnino, D. Iacopetta, R. Mazzotta, A. Caruso, M. R. Plutino, A. Mariconda, A. Ramunno, M. S. Sinicropi, V. Pezzi and P. Longo, *Bioorg. Med. Chem.*, 2015, **23**, 7302–7312.
19 A. Lin, C. J. Giuliano, A. Palladino, K. M. John, C. Abramowicz, M. L. Yuan, E. L. Sausville, D. A. Lukow, L. Liu, A. R. Chait, Z. C. Galluzzo, C. Tucker and J. M. Sheltzer, *Sci. Transl. Med.*, 2019, **11**, eaaw8412.
20 T. Chen, *Cancer Lett.*, 2024, **592**, 216931.
21 N. K. Sharma, A. Bahot, G. Sekar, M. Bansode, K. Khunteta, P. V. Sonar, A. Hebale, V. Salokhe and B. K. Sinha, *Cancers*, 2024, **16**, 680.
22 Q. Zhao, B. Han, C. Peng, N. Zhang, W. Huang, G. He and J.-L. Li, *Med. Res. Rev.*, 2024, **44**, 2194–2235.
23 J. Ceramella, A. Mariconda, D. Iacopetta, C. Saturnino, A. Barbarossa, A. Caruso, C. Rosano, M. S. Sinicropi and P. Longo, *Bioorg. Med. Chem. Lett.*, 2020, **30**, 126905.
24 C. Bonnefous, J. E. Payne, J. Roppe, H. Zhuang, X. Chen, K. T. Symons, P. M. Nguyen, M. Sablad, N. Rozenkrants, Y. Zhang, L. Wang, D. Severance, J. P. Walsh, N. Yazdani, A. K. Shiau, S. A. Noble, P. Rix, T. S. Rao, C. A. Hassig and N. D. Smith, *J. Med. Chem.*, 2009, **52**, 3047–3062.
25 J. Zuo, T.-H. Zhang, L. Xiong, L. Huang, C. Peng, Q.-M. Zhou and O. Dai, *Molecules*, 2022, **27**, 6102.
26 A. Inkanuwat, R. Sukaboon, O. Reamtong, P. Asawanonda, A. Pattaratanakun, T. Saisavoey, P. Sangtanoo and A. Karnchanatat, *Food Technol. Biotechnol.*, 2019, **57**, 200–212.

27 B. Hinz, K. Brune, T. Rau and A. Pahl, *Pharm. Res.*, 2001, **18**, 151–156.

28 M. D. Carrión, B. Rubio-Ruiz, F. Franco-Montalban, P. Amoia, M. C. Zuccarini, C. De Simone, M. E. Camacho, R. Amoroso and C. Maccallini, *Eur. J. Med. Chem.*, 2023, **248**, 115112.

29 A. J. Didier, J. Stiene, L. Fang, D. Watkins, L. D. Dworkin and J. F. Creeden, *Antioxidants*, 2023, **12**, 632.

30 Y. J. Oh, S. E. Jin, H.-K. Shin and H. Ha, *Sci. Rep.*, 2023, **13**, 18891.

31 D. Iacopetta, C. Costabile, M. La Chimia, A. Mariconda, J. Ceramella, D. Scumaci, A. Catalano, C. Rosano, G. Cuda, M. S. Sinicropi and P. Longo, *ACS Med. Chem. Lett.*, 2023, **14**, 1567–1575.

32 Y. Tian, S. Zhou, R. Takeda, K. Okazaki, M. Sekita and K. Sakamoto, *Biomed. Pharmacother.*, 2021, **141**, 111854.

33 A. Mariconda, D. Iacopetta, M. Sirignano, J. Ceramella, A. D'Amato, M. Marra, M. Pellegrino, M. S. Sinicropi, S. Aquaro and P. Longo, *Int. J. Mol. Sci.*, 2024, **25**, 2599.

34 D. R. Cheshire, A. Åberg, G. M. K. Andersson, G. Andrews, H. G. Beaton, T. N. Birkinshaw, N. Boughton-Smith, S. Connolly, T. R. Cook, A. Cooper, S. L. Cooper, D. Cox, J. Dixon, N. Gensmantel, P. J. Hamley, R. Harrison, P. Hartopp, H. Käck, P. D. Leeson, T. Luker, A. Mete, I. Millichip, D. J. Nicholls, A. D. Pimm, S. A. St-Gallay and A. V. Wallace, *Bioorg. Med. Chem. Lett.*, 2011, **21**, 2468–2471.

35 G. M. Morris, R. Huey, W. Lindstrom, M. F. Sanner, R. K. Belew, D. S. Goodsell and A. J. Olson, *J. Comput. Chem.*, 2009, **30**, 2785–2791.

36 M. F. Sanner, B. S. Duncan, C. J. Carrillo and A. J. Olson, in *Biocomputing '99*, World Scientific, 1998, pp. 401–412.

37 C. Rosano, R. Lappano, M. F. Santolla, M. Ponassi, A. Donadini and M. Maggiolini, *Curr. Med. Chem.*, 2012, **19**, 6199–6206.

38 E. F. Pettersen, T. D. Goddard, C. C. Huang, G. S. Couch, D. M. Greenblatt, E. C. Meng and T. E. Ferrin, *J. Comput. Chem.*, 2004, **25**, 1605–1612.